Available online at www.sciencedirect.com
SCIENCE DIRECT®
Journal of Solid State Chemistry 178 (2005) 1071–1079
JOURNAL OF SOLID STATE CHEMISTRY
www.elsevier.com/locate/jssc

Synthesis, structure and properties of the new rare-earth Zintl phase $Yb_{11}GaSb_9$

Svilen Bobev[a,*], Veronika Fritsch[b], Joe D. Thompson[b], John L. Sarrao[b], Bernhard Eck[c], Richard Dronskowski[c], Susan M. Kauzlarich[d]

[a]*Department of Chemistry and Biochemistry, University of Delaware, 304A Drake Hall, Newark, DE 19716, USA*
[b]*Los Alamos National Laboratory, MST-10/MS K764, Los Alamos, NM 87545, USA*
[c]*Institut für Anorganische Chemie, Rheinisch-Westfälische Technische Hochschule, 52056 Aachen, Germany*
[d]*Department of Chemistry, University of California, One Shields Avenue, Davis, California 95616*

Received 7 December 2004; accepted 11 January 2005

Abstract

A new rare-earth rich Zintl phase $Yb_{11}GaSb_9$ was synthesized by direct fusion of the corresponding elements, and large single crystals of the compound were obtained from high temperature flux synthesis. Its crystal structure was determined by single-crystal X-ray diffraction to be orthorhombic in the non-centrosymmetric space group *Iba*2 (No. 45), $Z = 4$ ($R_1 = 3.24\%$, w$R_2 = 6.40\%$) with $a = 11.7257(12)$ Å, $b = 12.3204(13)$ Å, $c = 16.633(2)$ Å measured at 90(3) K. The structure belongs to the $Ca_{11}InSb_9$-type and can be viewed as built of isolated Sb_4-tetrahedra centered by Ga, Sb-dimers and isolated Sb anions, which are separated by Yb^{2+} cations. Electron count according to the Zintl formalism suggests that the phase is electron-precise and charge-balanced, which is supported by the virtually temperature-independent magnetization for $Yb_{11}GaSb_9$. Electrical resistivity data from 2 to 400 K confirm that $Yb_{11}GaSb_9$ is a small band-gap semiconductor with room temperature resistivity $\rho_{298} = 45.1\,m\Omega\,cm$, and low-temperature resistivity at 2 K $\rho_2 = 1.9\,\Omega\,cm$. As such, $Yb_{11}GaSb_9$ and related compounds might be promising materials for thermoelectric applications, and currently, efforts to synthesize new members of this family and test their thermoelectric performance are under way.

Keywords: Rare-earth intermetallics; Crystal structure; Magnetic measurements; $Yb_{11}GaSb_9$; Heat capacity; DFT-calculations; Zintl phase

1. Introduction

In the past decade, polar intermetallic compounds formed between the electropositive alkaline-earth (Ca, Sr, Ba) and divalent rare-earth metals (Eu, Yb) with the early post-transition elements from group 13 (Al, Ga, In) and the pnicogens, i.e., group 15 (P, As, Sb, Bi) have been extensively studied [1–4]. In many of these compounds, in spite of the inherent structural complexity and diversity, simple electron counting rules such as the classic octet (8-N) rule have been found highly effective for rationalization of their structures and bonding [1–5]. This is done assuming complete transfer of valence electrons from the electropositive elements to the electronegative ones, and hence, the electropositive atoms could be viewed simply as spectator cations, while the electronegative atoms rearrange to form partial anionic sub-lattices with varying degrees of localized and/or delocalized bonding—widely known as Zintl concept [6].

Nevertheless, this simple-minded idea for rationalization of the formal electronic structure should be used very carefully—there are instances where interesting magnetic and electronic properties abound in seemingly closed-shell systems. For example, just the series of compounds $AE_{14}(M)Pn_{11}$ and $RE_{14}(M)Pn_{11}$ (AE = Ca, Sr, Ba; RE = Eu, Yb; M = Al, Ga, In, Zn, Mn; Pn = P,

*Corresponding author. Fax: +302 831 6335.
E-mail address: sbobev@chem.udel.edu (S. Bobev).

0022-4596/$ - see front matter © 2005 Elsevier Inc. All rights reserved.
doi:10.1016/j.jssc.2005.01.008

As, Sb, Bi) offers a wide range of properties ranging from semiconducting behavior, to large and/or colossal magnetoresistance, ferro-magnetism, mixed-valency, non-stoichimetry, etc. [7]. Using the classical Zintl approach, these structures can be viewed as built of discrete tetrahedral *M*-centered units, linear *Pn* trimers and isolated *Pn* ions, surrounded by divalent *AE* or *RE* cations. However, it has been demonstrated that this electron-counting scheme is overly simplistic in evaluating the complex physical properties of at least some of these phases (e.g., $Yb_{14}MnSb_{11}$) [8].

This remarkably rich and structurally diverse chemistry provided us with the motivation to continue studying similar materials and led us to the discovery of several novel compounds such as $Eu_{10}Mn_6Sb_{13}$ [9], $AE_{21}Mn_4Sb_{18}$ ($AE = Ca$, Sr) [10], $Yb_9Zn_{4+x}Sb_9$ and $Yb_9Mn_{4+x}Sb_9$ [11]. These novel Zintl phases, analogously to the "14-1-11"-compounds [7], also contain isolated antimony anions and/or polyanions, that are arranged in a comparable manner in respect to both the anionic and the cationic sub-structure. In all these new polar intermetallics, Zintl concept can be applied in a straightforward manner, although their properties are not necessarily consistent with the idealized charge-balanced compositions [7–11].

In order to unequivocally determine the electronic properties of the recently discovered $Yb_9Zn_{4+x}Sb_9$ (non-stoichiometric phase existing in a narrow homogeneity range $0.2 < x < 0.5$), we attempted to produce large single crystals of it from molten Ga flux. Instead, this reaction produced large single crystals of the new rare-earth rich Zintl phase $Yb_{11}GaSb_9$ ($Ca_{11}InSb_9$-type) [12]. Herein, we report on the structural characterization, bonding and properties of this new material, whose structure is closely related to the "14-1-11" structure-type [7].

2. Experimental section

2.1. Synthesis

All manipulations were performed under vacuum or in an inert atmosphere. The starting materials (pure elements) were used as received. Yb (pieces, Ames 99.9%), Ga (ingot, Alfa, 99.999%), and Sb (ingot, Alfa 99.99%) were loaded with the desired stoichiometric ratios in either 5 or 2 cm^3 alumina crucibles, which were then put in fused silica ampoules. The ampoules were in turn closed under vacuum (or high purity Ar at 1/5 atm) by flame sealing.

Initially, single crystals of $Yb_{11}GaSb_9$ were obtained from a reaction loaded as $Yb_9Zn_{4.5}Sb_9Ga_x$ ($x > 50$), which was intended to produce large single crystals of the non-stoichiometric $Yb_9Zn_{\sim 4.5}Sb_9$ from a molten Ga solution [11]. The reaction mixture was heated in a programmable muffle furnace using the following temperature profile: (1) quick ramping (150 °C/h) to 1000 °C, dwell at that temperature for 24 h, followed by slow cooling (–5 °C/h) to 600 °C. At that point, the excess Ga was removed by centrifugation. Details on the flux-growth synthetic procedures have been discussed in detail elsewhere [13].

After the structure and the composition were established from single crystal X-ray diffraction work, the synthesis of $Yb_{11}GaSb_9$ was successfully reproduced from pure elements in stoichiometric fashion. The mixtures were typically heated at 800–1000 °C and were always allowed to slowly cool down. The reactions were carried out in Al_2O_3-crucibles and/or sealed Ta-tubes, jacketed in evacuated fused-silica ampoules. Powder X-ray diffraction however indicated that the "on-stoichiometry" reaction outcomes contained trace amounts of impurity phases—$Yb_{11}Sb_{10}$ and Yb_4Sb_3 [14], below 5–10% by weight (est.).

Large single crystals of the title compound in quantitative yields were produced from reactions of Yb and Sb in Ga flux (reactions were loaded as $Yb_{11}Ga_xSb_9$ ($x \sim 70$) and the above-mentioned temperature profile for flux growth was employed). Irregularly shaped crystals with silver-metallic luster, some of them very large (up to ca. 7–9 mm) were isolated, cleaned from the excess Ga by sonification in warm water, and used for the precise structure determination and for the physical properties measurements. The crystals of $Yb_{11}GaSb_9$ appear stable in air, but dissolve readily in mineral acids. Despite the seeming stability, our property measurement data suggest the presence of trace amounts of Yb_2O_3, an indication for a slow sample oxidation (below).

2.2. Powder X-ray diffraction

X-ray powder diffraction patterns were used to monitor the reaction outcomes and were taken at room temperature on a Scintag XDS 2000 powder diffractometer equipped with monochromatized Cu $K\alpha$ radiation. The PXRD data analysis was carried out employing the MDI-JADE 6.5 software package [15]. The diffraction patterns were compared with those calculated from the single-crystal data using the Crystal Diffract 4.1 package [16]. Powder patterns of crushed crystals of $Yb_{11}GaSb_9$ before and after exposure to air showed no signs of decomposition products, indicating that the title compound is stable in dry air (*note: an indication for traces of impurity Yb_2O_3 in all our samples is evidenced from the calorimetry and magnetization data (below), but the estimated amount of Yb_2O_3 is ~0.1%—well below the detectable limits*). The X-ray powder patterns were not used for determination of the unit cell parameters because of the relatively low symmetry and large cell constants (Table 1). The lattice parameters for different samples (determined from single-crystal X-ray

Table 1
Selected crystallographic data for $Yb_{11}GaSb_9$

Chemical formula	$Yb_{11}GaSb_9$
Formula weight	3068.91
Space group, Z	*Iba*2 (No. 45), 4
Unit cell parameters	$a = 11.7257(12)$ Å
	$b = 12.3204(13)$ Å
	$c = 16.633(2)$ Å
	$V = 2402.9(4)$ Å^3
Radiation, λ (Å)	Mo$K\alpha$, 0.71073
Temperature, T (K)	90(3)
θ range for data collection (°)	2.4–30.8
Reflections collected/unique	10566/3708 [$R_{int} = 4.77\%$]
Crystal size (mm)	$0.10 \times 0.06 \times 0.05$
Data/restraints/parameters	3708/1/99
ρ_{calcd} (g/cm^3)	8.483
μ (cm^{-1})	533.16
Absorption correction method	Multi-scan
Flack parameter	0.03(1)
Goodness of fit on F^2	1.069
Final R_1 ($I > 2\sigma_I$)[a]	3.24%
Final wR_2 ($I > 2\sigma_I$)[b]	6.40%

[a] $R_1 = \sum||F_o|-|F_c||/\sum|F_o|$.
[b] $wR_2 = [\sum[w(F_o^2-F_c^2)^2]/\sum[w(F_o^2)^2]]^{1/2}$, and
$w = 1/[\sigma^2F_o^2 + (0.0148P)^2 + 9.721P]$, $P = (F_o^2 + 2F_c^2)/3$.

diffraction), synthesized under different condition, with or without flux, showed no differences, which confirms that $Yb_{11}GaSb_9$ is a line compound.

2.3. Single crystal X-ray diffraction

Intensity data were collected for a flux-grown crystal of $Yb_{11}GaSb_9$ (dark-metallic, $0.10 \times 0.06 \times 0.05$ mm), selected and mounted on a glass fiber under Exxon Paratone N oil. The crystal was then placed under the cold nitrogen stream (ca. −180 °C) of a Bruker SMART 1000 CCD diffractometer equipped with a low-temperature apparatus. A sphere of data was collected using graphite monochromatized Mo$K\alpha$ radiation (10 s exposure time per frame, 0.3° ω-scans, $2\theta_{max} \sim 61°$, 10,566 total reflections, 3708 unique reflections, $R_{int} = 4.77\%$). The data were corrected for Lorentz and polarization effects and integrated in Laue symmetry of *mmm* using the SMART and SAINT software, respectively [17]. Multi-scan absorption correction was applied with the aid of the SADABS software package [18].

The presence of reflections with $h + k + l = 2n$ readily confirmed the body-centering, and the systematic absence conditions, $0kl$ for $k \neq 2n$; $l \neq 2n$, $h0l$ for $h \neq 2n$; $l \neq 2n$, $hk0$ for $h + k \neq 2n$, suggested only two possible space groups—the non-centrosymmetric *Iba*2 (No. 45) and the centrosymmetric *Ibam* (No. 72). Structure solution and refinement was attempted in both space groups, and this unambiguously proved that the non-centrosymmetric *Iba*2 is the correct one. Moreover, review of the current literature revealed a similarity of the unit cell parameters of $Yb_{11}GaSb_9$ ($a \sim 11.7$ Å, $b \sim 12.3$ Å, $c \sim 16.6$ Å at 90 K), and those of $Ca_{11}GaSb_9$ ($Ca_{11}InSb_9$ structure type [12,14]; Pearson's code o*I*84; space group *Iba*2; $a \sim 11.8$ Å, $b \sim 12.5$ Å, $c \sim 16.7$ Å at 130 K) [19], and implied that the new rare-earth rich compound and the Zintl phase $Ca_{11}GaSb_9$ are isostructural. This further confirmed the space group choice and provided the initial structure model.

Table 2
Atomic coordinates and equivalent isotropic displacement parameters (U_{eq}[a]) for $Yb_{11}GaSb_9$

Atom	Site	x	y	z	U_{eq} (Å^2)
Sb1	8*c*	0.12856(6)	0.88627(7)	0.49671(6)	0.0057(1)
Sb2	4*b*	0	$\frac{1}{2}$	0.74877(9)	0.0052(1)
Sb3	8*c*	0.82120(7)	0.82242(8)	0.31744(6)	0.0059(2)
Sb4	8*c*	0.53533(6)	0.89052(7)	0.50246(7)	0.0060(1)
Sb5	8*c*	0.85330(7)	0.86212(8)	0.68988(5)	0.0057(2)
Ga1	4*a*	0	0	0.6077(1)	0.0081(4)
Yb1	8*c*	0.57016(5)	0.77592(5)	0.34116(4)	0.0058(1)
Yb2	8*c*	0.31492(5)	0.77181(5)	0.37145(4)	0.0072(1)
Yb3	8*c*	0.58975(5)	0.77181(5)	0.65864(4)	0.0065(1)
Yb4	8*c*	0.31401(5)	0.93880(6)	0.62946(4)	0.0079(1)
Yb5	8*c*	0.16141(4)	0.82806(5)	0.00146(5)	0.0077(1)
Yb6	4*a*	0	0	0.32330(5)	0.0080(1)

[a] U_{eq} is defined as 1/3 of the trace of the orthogonalized U_{ij} tensor.

The $Yb_{11}GaSb_9$ structure was subsequently refined on F^2 using the SHELXTL V5.1 package [20]. The first least-square cycles when all atoms were refined with isotropic atomic displacement parameters (U's hereafter) easily converged and confirmed the model. Next, all U's were refined anisotropically, the R_1 and wR_2 factors dropped to 3.24% and 6.40% (99 parameters and 3460 structure factors $F > 4\sigma_F$), respectively, with no peaks of significant height present in the difference Fourier map (± 3 e$^-$/Å^3). All 12 refined positions had well-behaved thermal parameters, and were proven to be fully occupied with corresponding deviations within 4σ from the full occupancy. Important data collection and structure refinements parameters for $Yb_{11}GaSb_9$ are given in Table 1; positional and equivalent isotropic displacement parameters and important bond distances for $Yb_{11}GaSb_9$ are listed in Tables 2 and 3, respectively. Further details of the crystal structure investigation can be obtained from the Fachinformationszentrum Karlsruhe, 76344 Eggenstein-Leopoldshafen, Germany (fax: (49) 7247-808-666; e-mail: crysdata@fiz.karlsruhe.de) on quoting the depository number CSD 414633.

2.4. Magnetic susceptibility measurements

The dc magnetic susceptibility ($\chi(T) = M/H$) measurements were performed in a Quantum Design MPMS SQUID magnetometer from 2 to 350 K. Different reaction batches were measured in order to provide

Table 3
Important bond distances (Å) in $Yb_{11}GaSb_9$

Atom pair		Distance	Atom pair		Distance
Sb1–	Ga1	2.765(2)	Yb1–	Sb3	3.025(1)
	Yb2	3.107(1)		Sb4	3.059(1)
	Yb4	3.166(1)		Sb5	3.167(1)
	Yb1	3.340(1)		Sb3	3.185(1)
	Yb3	3.355(1)		Sb2	3.265(1)
	Yb5	3.476(1)		Sb1	3.340(1)
	Yb5	3.542(1)	Yb2–	Sb2	3.053(1)
	Yb6	3.543(1)		Sb1	3.107(1)
	Yb5	3.611(1)		Sb3	3.392(1)
Sb2–	2 × Yb4	3.044(1)		Sb3	3.426(1)
	2 × Yb2	3.053(1)		Sb4	3.448(1)
	2 × Yb1	3.265(1)		Sb4	3.449(1)
	2 × Yb3	3.355(1)		Sb5	3.752(1)
Sb3–	Yb1	3.025(1)	Yb3–	Sb4	3.049(1)
	Yb6	3.032(1)		Sb3	3.068(1)
	Yb3	3.068(1)		Sb5	3.268(1)
	Yb5	3.068(1)		Sb5	3.325(1)
	Yb1	3.185(1)		Sb1	3.355(1)
	Yb2	3.392(1)		Sb2	3.355(1)
	Yb2	3.426(1)		Ga1	3.611(1)
	Yb4	3.787(1)	Yb4–	Sb2	3.044(1)
Sb4–	Sb4	2.822(2)		Sb1	3.166(1)
	Yb3	3.049(1)		Sb5	3.298(1)
	Yb1	3.059(1)		Sb4	3.399(1)
	Yb4	3.399(1)		Sb4	3.465(1)
	Yb2	3.448(1)		Ga1	3.776(1)
	Yb2	3.449(1)		Sb3	3.787(1)
	Yb4	3.465(1)		Sb5	3.869(1)
	Yb5	3.546(1)	Yb5–	Sb3	3.068(1)
	Yb5	3.638(1)		Sb5	3.167(1)
Sb5–	Ga1	2.777(1)		Ga1	3.346(1)
	Yb5	3.167(1)		Sb1	3.476(1)
	Yb1	3.167(1)		Sb1	3.542(1)
	Yb3	3.268(1)		Sb4	3.546(1)
	Yb6	3.282(1)		Sb1	3.611(1)
	Yb4	3.298(1)		Sb4	3.638(1)
	Yb3	3.325(1)	Yb6–	2 × Sb3	3.032(1)
	Yb2	3.752(1)		2 × Sb5	3.282(1)
	Yb4	3.869(1)		2 × Sb1	3.543(1)
Ga1–	2 × Sb1	2.765(2)		Ga1	3.586(2)
	2 × Sb5	2.777(1)		2 × Yb1	3.510(1)
	2 × Yb5	3.346(1)			

reproducible results. All samples were measured in field cooling mode at a magnetic field of 0.1 T. The specimens were large single crystals (approximately 10–20 mg), which were secured between two pieces of quartz wool and loaded in plastic straws. The raw data were corrected for the contribution of the holder and converted to molar susceptibility. In order to determine the Yb formal oxidation, molar susceptibility was normalized per mole of Yb.

2.5. Resistivity and heat capacity measurements

The electrical resistivity measurements were carried out on a Quantum Design PPMS system using a four-probe technique from 1.8 to 400 K with applied current of 1 mA. Resistance as a function of temperature and field up to 5 T was measured on four different samples (single crystals, previously used in the magnetization measurements), again to assure reproducibility and consistent results. Selected well-shaped crystals, typically 3–5 mm in size, were carefully sand-polished immediately before attaching the 0.002″ Pt-wire leads to the surface using Ag epoxy. This was done in order to minimize the ohmic resistance from surface impurities/oxidation. The specific heat for the very same samples was determined in a He^4 cryostat with a home-built setup in the temperature range 1.3–20 K using thermal relaxation techniques.

2.6. Electronic structure calculations

Total-energy electronic structure calculations of the density-functional type on $Ca_{11}GaSb_9$ and $Yb_{11}GaSb_9$ were performed using the full-potential linearized augmented-plane-wave (FLAPW) method as implemented in the WIEN2k program package [21]. The calculations where based on the generalized-gradient approximation (GGA) with an exchange-correlation potential as proposed by Perdew, Burke, and Ernzerhof [22]. The muffin-tin radii were set to 2.6 Bohr for all the atoms, and the valence states, expanded up to $l = 10$ in terms of angular momenta, were treated scalar-relativistically. The number of irreducible k points was 45, and the total energy was converged to less than 0.0001 Ry.

3. Results and discussion

3.1. Structure description

As already mentioned, the structure of $Yb_{11}GaSb_9$ belongs to the $Ca_{11}InSb_9$ structure type [12], which has already been discussed elsewhere. Herein we turn attention to some details of the coordination and bonding of the rare-earth elements in connection with the properties of this new rare-earth rich compound (below).

The $AE_{11}TrPn_9$ family of polar intermetallic phases (AE = Ca, Sr, Ba, Yb; Tr = Triel = Al, Ga, In; Pn = Pnicogen = Sb, Bi) is representative of the Zintl phases and the structure can be rationalized using the classic valence rules and is best described in terms of discrete Ga-centered tetrahedra of Sb, isolated Sb dimers, and isolated Sb atoms. These anionic species are separated by the AE^{2+} cations, which occupy the empty space between them (Fig. 1), and counterbalance the charges. In that sense, following the Zintl formalism and rules for electron counting, the formula $Yb_{11}GaSb_9$

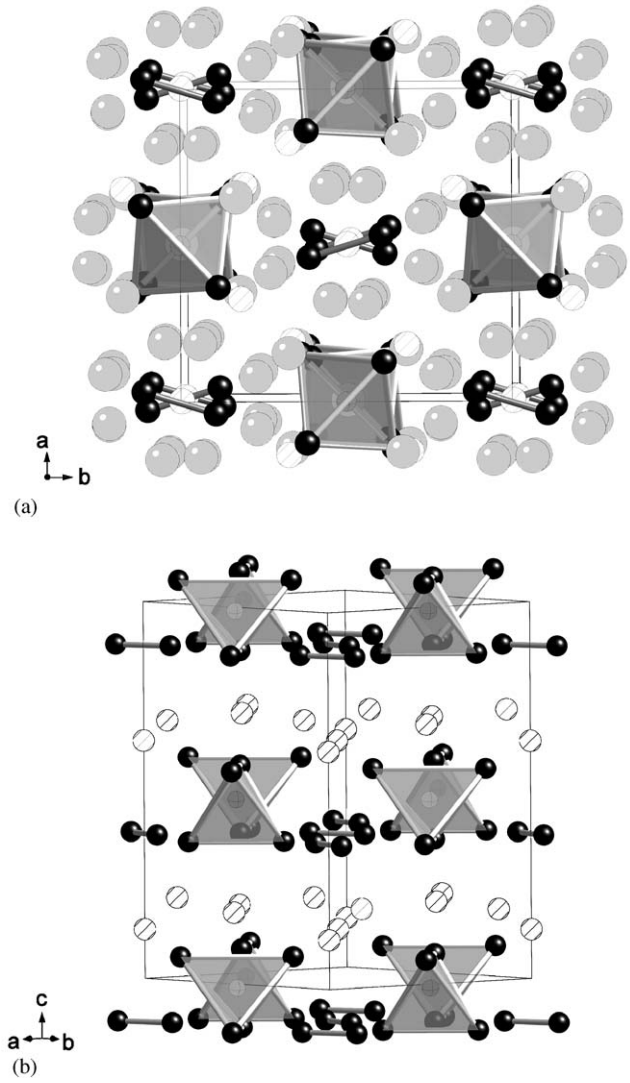

Fig. 1. (a) Representation of the orthorhombic structure of $Yb_{11}GaSb_9$ viewed down the *c*-axis (unit cell is outlined). The Yb atoms are shown as large gray spheres, the isolated Sb atoms are shown as small striped circles, while the Sb_2^{4-} dimers are drawn in black. The Ga atoms that center the $GaSb_4^{9-}$ tetrahedra are highlighted in the translucent gray polyhedra. (b) The structure of $Yb_{11}GaSb_9$ viewed along [110] direction. All Yb cations are omitted for clarity. The acentric arrangement of the building units is clearly seen from that projection.

can be broken down to:

$$Yb_{11}GaSb_9 = 11 \times Yb^{2+} + GaSb_4^{9-} + Sb_2^{4-} + 3 \times Sb^{3-}.$$

As can be seen from Fig. 1, the $GaSb_4^{9-}$ tetrahedra and the Sb_2^{4-} dimers are arranged in alternating fashion with isolated Sb^{3-} anions in a direction of the *c*-axis. The dimers and the tetrahedra are also stacked in an eclipsed fashion as they alternate along the *a*- and *b*-directions, respectively. Similar structural motifs and packing arrangements are known for the "14-1-11" structure-type ($AE_{14}(M)Pn_{11}$ and $RE_{14}(M)Pn_{11}$ compounds, where AE = Ca, Sr, Ba; RE = Eu, Yb; M = Al, Ga, In, Zn, Mn; Pn = P, As, Sb, Bi), where instead of dimers, linear Pn_3^{7-} polyanions are present, and they are similarly coordinated [7].

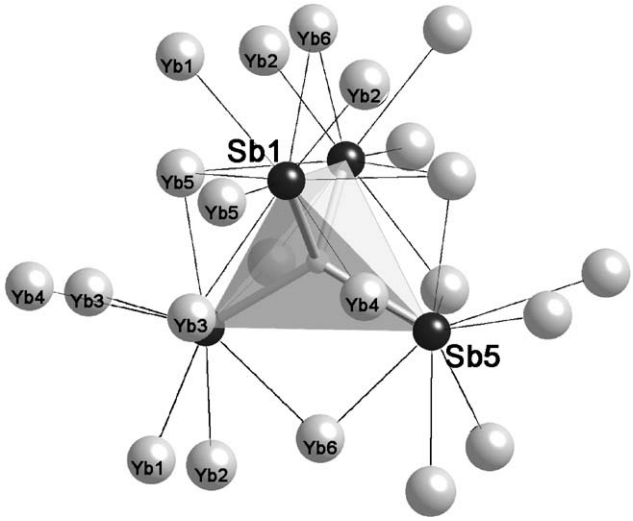

Fig. 2. Coordination environment of the $GaSb_4^{9-}$ tetrahedra in $Yb_{11}GaSb_9$. Emphasized is the way the Yb^{2+} cations cap corners, edges and faces of the $GaSb_4^{9-}$ tetrahedron. Each Sb-atom has eight next-nearest neighbors ($d < 3.9$ Å). The closest Ga–Yb distance is 3.346(1) Å—between Ga and Yb5, respectively.

The Ga-centered Sb_4 tetrahedra (Fig. 2) are built of two crystallographically inequivalent Sb atoms, Sb2 and Sb5 (Table 2), yet the corresponding Ga–Sb bonding distances are very similar; 2.765(2) and 2.771(1) Å for Ga1–Sb1 and Ga1–Sb5, respectively (Table 3). In spite of the different temperatures at which X-ray data have been collected, these distances compare very well with Ga–Sb distances in other polar intermetallics ($Ca_{11}GaSb_9$, 2.76 Å; $Ca_5Ga_2Sb_6$, 2.72 Å; $REGaSb_2$, 2.75 Å) [23,24]. For that matter, the Sb–Ga–Sb tetrahedral angles in $Yb_{11}GaSb_9$, which deviate somewhat from the ideal value of 109.5°, 107.51(3)° and 110.87(3)°, respectively, also compare very well with the Sb–Ga–Sb tetrahedral angles reported in the above-mentioned Zintl phases.

The $GaSb_4^{9-}$ tetrahedra in $Yb_{11}GaSb_9$ are well separated; they are 8.316(1) Å apart from each other (center to center), and 5.137(1) Å away from the next nearest Sb_2^{4-} dimer. Each of the Sb-vertices is coordinated by 8 next-nearest Yb's, in a way that the whole tetrahedral unit is thoroughly surrounded and shielded by 22 Yb^{2+} cations (Fig. 2). These cap corners, edges and faces with Yb–Sb distances ranging from 3.107(1) to 3.611(1) Å for Yb–Sb1, and from 3.167(1) to 3.869(1) Å for Yb–Sb5, respectively.

The Sb–Sb bond distance in the Sb_2^{4-} dimer is 2.822(2) Å (Table 3). Compared to elemental Sb (2.908 Å) and other polar intermetallics with direct Sb–Sb bonding: $Yb_{11}Sb_{10}$ [25], $Ca_{11}Sb_{10}$ [26], and

$Sr_{11}Sb_{10}$ (2.95–3.36 Å) [27], REGaSb$_2$ (3.0–3.1 Å) (23); $RE_{12}Ga_4Sb_{23}$ (3.0–3.15 Å) [28], for example, this shorter contact suggests much stronger and localized interactions between the antimony atoms in that case. Similar Sb–Sb bond distances are found in the classic Zintl phases $Ca_{11}GaSb_9$ (2.831 Å) and $Ca_5Ga_2Sb_6$ (2.84 Å) [19,24]. All these indicate that the Sb_2^{4-} dimer in $Yb_{11}GaSb_9$ exhibits normal 2-center-2-electron bonding. In comparison, the linear Sb_3^{7-} polyanions in the structurally similar "14-1-11" phases have Sb–Sb bond distances in the order of 3.2 Å. These weakly bonding interactions are often described as hypervalent 3-center-4-electron, i.e., isoelectronic with I_3^- anions [7], whereas the Sb_2^{4-} dumbbell can be regarded as isolectronic with the I_2 molecule.

The Sb_2^{4-} dimer is tightly coordinated by 12 next-nearest Yb's (Fig. 3) at distances varying from 3.049(1) to 3.638(1) Å. Each of the Sb atoms has a CN of 8 in a square-antiprismatic fashion. These Yb–Sb distances and Sb-coordination are very similar to the Sb environment found for the discrete $GaSb_4^{9-}$ tetrahedra (above). The isolated Sb^{3-} anions are also coordinated by eight adjacent ytterbium cations at distances in the range from 3.044(1) to 3.355(1) Å, and from 3.025(1) to 3.787(1) Å, for Yb–Sb2 and Yb–Sb3, respectively (Table 3).

The six crystallographically different Yb cations occupy the space between the tetrahedra, dimers, and isolated Sb atoms (Fig. 1), and have rather distinct coordination environments. All ytterbium atoms are packed in distorted octahedral or pentagonal bipyramidal fashion by 6 or 7 Sb atoms, respectively. Each of the faces of the Sb square- or pentagonal bipyramids is capped in turn by adjacent Yb's or Ga atoms. The corresponding Yb–Ga, and Yb–Sb bond distances (Table 3) fall in the range from 3.346(1) to 3.661(1) Å for Yb–Ga, and from 3.025(1) to 3.869(1) Å for Yb–Sb, respectively.

3.2. Properties

The physical properties measurements obtained on a number of samples made with different synthetic methods are consistent with the presence of trace amounts of Yb_2O_3, an indication for slow surface oxidation.

Field cooling magnetization data of three different "flux-grown" and one "on-stoichiometry" reaction batches of $Yb_{11}GaSb_9$ were obtained to ensure reproducible results. In the temperature range 50–350 K (Fig. 4) the magnetic susceptibility is nearly temperature independent and weakly paramagnetic, as expected from the Hund's rules for divalent Yb with $\mu_{eff} = 0$ [29]. Below 50 K, an impurity contribution is present, due to the small amounts of Yb_2O_3 (all measurements were done in ambient atmosphere). If the impurities were

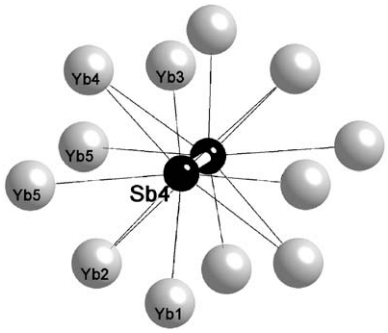

Fig. 3. The local coordination of the interstitial Sb_2^{4-} dimer. The corresponding bond distances are given in Table 3.

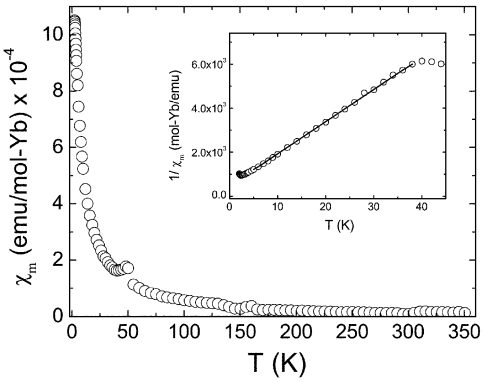

Fig. 4. Temperature dependence of the magnetic susceptibility (χ_m) of $Yb_{11}GaSb_9$. Measurements were performed on a flux-grown single crystal in a magnetic field of 0.1 T.

assumed all to be Yb^{3+}, an estimate of the volume fraction of Yb^{3+} in the sample can be made. With this assumption, the low-temperature susceptibility can be understood as arising from the presence of less than 0.1% Yb^{3+}. These considerations strongly indicate that in the $Yb_{11}GaSb_9$ structure, just like in the Ca-counterpart, all cations, i.e., all Yb's are divalent. This conclusion is fully supported from the electronic structure calculations.

Fig. 5 displays the specific heat of $Yb_{11}GaSb_9$ in the representation C/T vs. T. In agreement with the susceptibility data at $T = 2.2$ K a small transition can be observed, confirming the presence of antiferromagnetic Yb_2O_3 in the sample [30]. Beneath the magnetic contributions of this impurity phase to the specific heat, for $Yb_{11}GaSb_9$ only a lattice contribution to the specific heat is expected. To obtain the Debye temperature Θ_D of $Yb_{11}GaSb_9$ the inset of Fig. 4 enlarges its specific heat in the temperature range between 1.3 and 5 K. The data are shown in the representation $C/T^{3/2}$ vs. $T^{3/2}$. In this way, for sufficient low temperatures $T < \Theta_D/50$, the specific heat is a straight line, where the lattice contribution, which is $\propto T^3$, is represented by the slope of the curve ($\beta = 3.88$ mJ/mol K^4). The Debye

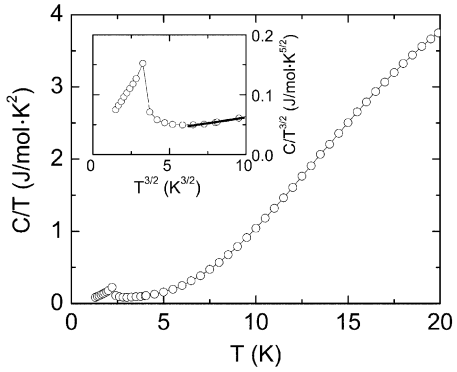

Fig. 5. Specific heat data of $Yb_{11}GaSb_9$ in the temperature range 1.3–20 K (represented in the form of C/T vs. T). Inset: specific heat of $Yb_{11}GaSb_9$ in the representation $C/T^{3/2}$ vs. $T^{3/2}$ in the temperature range between 1.3 and 5 K. The solid line is the linear fit used to determine the Debye temperature.

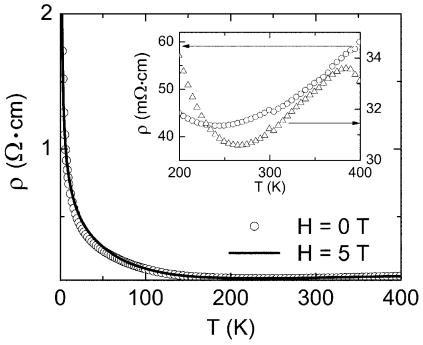

Fig. 6. Resistivity of $Yb_{11}GaSb_9$ in a magnetic field $H = 0$ T (circles) and $H = 5$ T (solid line). Inset: resistivity of two different single crystals of $Yb_{11}GaSb_9$ (the same batch) in the temperature range between 200 and 400 K.

temperature calculated from the slope is $\Theta_D = 219$ K, but because of the fact that the linear fit is in a very limited temperature range only, this value has to be considered simply as a rough approximation. Nevertheless, Debye temperatures in the order of 200 K are reported for other polar Yb–Sb and Yb–*M*–Sb intermetallics, such as Yb_4Sb_3 and $Yb_{14}ZnSb_{11}$, for example [7f,31].

Resistance was measured using the four-probe technique on four flux-grown single crystals of $Yb_{11}GaSb_9$. A representative plot of the electrical resistivity as a function of the temperature (1.8–400 K) for $Yb_{11}GaSb_9$ is shown in Fig. 6. The resistivity increases with decreasing temperature, suggesting semiconducting behavior, as expected for charge-balanced compound, i.e., a classical Zintl phase. Similar temperature dependence was reported for the isostructural and isoelectronic $Ca_{11}GaSb_9$, although its resistance is orders of magnitude higher [19]. At the lowest achieved temperature (1.8 K) the resistivity of $Yb_{11}GaSb_9$ reaches almost 2 Ω cm, nearly 40 times higher than its room temperature value of 45.1 mΩ cm. All attempts to describe the curve with an exponential law, either an Arrhenius- or a variable range hopping law, failed. This lead us to the conclusion that pure $Yb_{11}GaSb_9$ probably would exhibit a thermally activated behavior—in other words, the resistivity of the pure $Yb_{11}GaSb_9$ will follow an Arrhenius-law, but when there are impurities in the gap, an unusual temperature dependence of the resistivity is observed (our case). This assumption is corroborated by the apparent "sample-dependence" of the resistivity: the mininum's temperature of the resisitivity for two different pieces of the same batch differs about 30 K, as is illustrated in the inset of Fig. 6. As discussed in Section 2, and based on the strong evidence for Yb_2O_3 from the calorimetry and magentization measurements (above), small amounts of impurity Yb^{3+} in the samples is the most-likely reason for this "sample-dependence" and the corresponding departures from the Arrhenius-type behavior. These results are further corroborated by the electronic structure calculations (below).

Temperature dependence of the resistivity of $Yb_{11}GaSb_9$ in the presence of a magnetic field was also studied. The solid line in the main frame of Fig. 6 depicts the resistivity in a magnetic field $H = 5$ T. As evident from the plot, the magnetic field has no significant impact on the resistivity—a magnetoresistance of ~5% only was obtained at the lowest temperature.

3.3. Bonding and electronic band structure

The total and local densities-of-states for $Ca_{11}GaSb_9$ and $Yb_{11}GaSb_9$ are given in the left and right parts of Fig. 7. The Ca phase turns out to be a semiconductor, and the theoretical band gap of approx. 0.7 eV is extremely close to the experimental value of 0.64 eV determined earlier from conductivity measurement [19]. Because the density-functional result cannot be expected to yield reliable estimates of such an excited-state property, the numerical proximity of the two values can only be considered accidental. As expected from the Zintl–Klemm concept, Ca has lost its valence electrons almost entirely, and the orbital contributions of Ca are largely restricted to the virtual DOS region; below the Fermi level, the Ca mixing (black projected DOS) is quite small.

The calculated electronic structure of the Yb phase (right figure) turns out to be almost superimposable with one of the Ca-counterpart, the only exception being the sharp and fully occupied ytterbium 4*f* peak just below the Fermi level. In accord with the magnetic measurements, the minimum total energy is achieved for a non-spin-polarized approach, that is, with zero local moments on Yb and a formal $4f^{14}$ configuration. Although the figure alludes to a metallic phase, this finding is a graphical artifact that goes back to the small

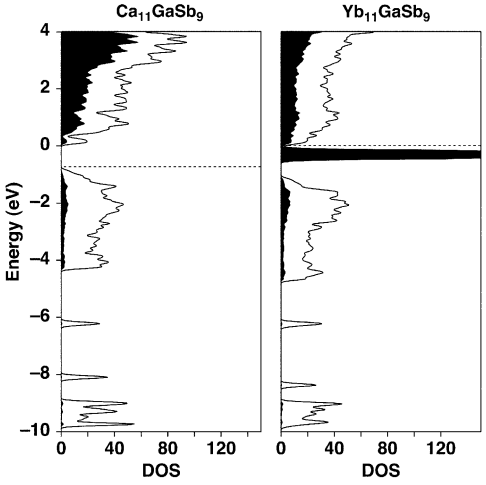

Fig. 7. Total and projected densities-of-states for $Ca_{11}GaSb_9$ (left) and $Yb_{11}GaSb_9$ (right) based on full-potential electronic-structure calculations and the GGA; Ca and Yb contributions are given in black. The Fermi levels are indicated by dashed horizontal lines.

Gaussian broadening used in the DOS presentation. In fact, a numerical inspection of the energy eigenvalues indicates that the filled 4*f* levels of Yb are separated from the virtual levels by a tiny energy gap of approx. 0.03 eV, indicating a narrow band-gap semiconductor. Experience suggests that the present density-functional approach probably overestimates the itinerancy of the 4*f* levels, and we suspect that the true band gap is indeed a little larger but still smaller than that of the Ca phase.

4. Conclusions

We have synthesized and structurally characterized a new ternary intermetallic phase, $Yb_{11}GaSb_9$, isostructural and isoelectronic with the previously reported Zintl phases $Ca_{11}MSb_9$ (M = Al, Ga, In). This new material provides another example of a rare-earth rich compound with complicated structure that can be rationalized using classical approaches such as the Zintl concept. Our experimental and theoretical studies confirm that $Yb_{11}GaSb_9$ is a closed-shell compound, hence, a small band-gap semiconductor, where all Yb-atoms are divalent. As such, $Yb_{11}GaSb_9$ and related Eu^{2+} compounds might be promising materials for thermoelectric applications. Preliminary data indicate this material is prone to doping with Zn and Mn on the Ga site, and currently, efforts to synthesize new members of this family and test their thermoelectric performance are under way.

Acknowledgments

Svilen Bobev acknowledges the Institute for Complex Adaptive Matter (ICAM) and the University of Delaware for the financial support of this work. Work at LANL was done under the auspices of US DOE. SMK acknowledges NSF for funding.

References

[1] H. Schäfer, B. Eisenmann, W. Müller, Angew. Chem. Int. Ed. Engl. 12 (1973) 694.
[2] (a) H.-G. von Schnering, Angew. Chem. Int. Ed. Engl. 20 (1981) 33;
(b) H. Schäfer, Ann. Rev. Mater. Sci. 15 (1985) 1.
[3] S.M. Kauzlarich (Ed.), Chemistry, Structure, and Bonding of Zintl Phases and Ions, VCH Publishers, Inc., New York, NY, 1996, and the references therein.
[4] (a) J.D. Corbett, Struct. Bonding 87 (1997) 157;
(b) J.D. Corbett, Angew. Chem. Int. Ed. 39 (2000) 670.
[5] R. Nesper, Angew. Chem. Int. Ed. Engl. 30 (1991) 789.
[6] E. Zintl, Angew. Chem. 52 (1939) 1.
[7] (a) R.F. Gallup, C.Y. Fong, S.M. Kauzlarich, Inorg. Chem. 31 (1992) 115;
(b) J.Y. Chan, M.M. Olmstead, S.M. Kauzlarich, D.J. Webb, Chem. Mater. 10 (1998) 3583;
(c) J.Y. Chan, M.E. Wang, A. Rehr, S.M. Kauzlarich, Chem. Mater. 9 (1997) 2131;
(d) J.Y. Chan, S.M. Kauzlarich, P. Klavins, R.N. Shelton, D.J. Webb, Chem. Mater. 9 (1997) 3132;
(e) J.Y. Chan, S.M. Kauzlarich, P. Klavins, R.N. Shelton, D.J. Webb, Phys. Rev. B 57 (1998) 8103;
(f) I.R. Fisher, S.L. Bud'ko, C. Song, P.C. Canfield, T.C. Ozawa, S.M. Kauzlarich, Phys. Rev. Lett. 85 (2000) 1120.
[8] A.P. Holm, S.M. Kauzlarich, S.A. Morton, G.D. Waddill, W.E. Pickett, G. Tobin, J. Am. Chem. Soc. 124 (2002) 9894.
[9] A.P. Holm, S.-M. Park, C.L. Condron, M.M. Olmstead, H. Kim, P. Klavins, F. Grandjean, R.P. Hermann, G.J. Long, M.G. Kanatzidis, S.M. Kauzlarich, S.-J. Kim, Inorg. Chem. 42 (2003) 4660.
[10] (a) H. Kim, C.L. Condron, A.P. Holm, S.M. Kauzlarich, J. Am. Chem. Soc. 122 (2000) 10720;
(b) A.P. Holm, M.M. Olmstead, S.M. Kauzlarich, Inorg. Chem. 42 (2003) 1973.
[11] (a) S. Bobev, J.D. Thompson, J.L. Sarrao, M.M. Olmstead, H. Hope, S.M. Kauzlarich, Inorg. Chem. 43 (2004) 5044
(b) S. Bobev, unpublished.
[12] G. Cordier, H. Schäfer, M. Stelter, Z. Naturforsch. 40b (1985) 868.
[13] P.C. Canfield, Z. Fisk, Philos. Mag. B 65 (1992) 1117.
[14] P. Villars, L.D. Calvert (Eds.), Pearson's Handbook of Crystallographic Data for Intermetallic Phases, ASM International, Materials Park, OH, 1991, and the desktop edition, 1999.
[15] JADE Version 6.5, Materials Data, Inc., Livermore, CA, 2003.
[16] CrystalDiffract Version 4.1, CrystalMaker Sofwtare, Bicester, Oxfordshire, UK, 2003.
[17] (a) SMART NT Version 5.05, Bruker Analytical X-ray Systems, Inc., Madison, WI, 1998;
(b) SAINT NT Version 6.22, Bruker Analytical X-ray Systems, Inc., Madison, WI, 2001.
[18] SADABS NT Version 2.05, Bruker Analytical X-ray Systems, Inc., Madison, WI, 1998.
[19] D.M. Young, S.M. Kauzlarich, Chem. Mater. 7 (1995) 206.
[20] SHELXTL Version 5.10, Bruker Analytical X-ray Systems, Inc., Madison, WI, 1997.
[21] P. Blaha, K. Schwarz, G.K.H. Madsen, D. Kvasnicka, J. Luitz, WIEN2K, An Augmented Plane Wave and Local Orbitals Program for Calculating Crystal Properties, Technische Universität Wien, Austria, 2001.

[22] J.P. Perdew, K. Burke, M. Ernzerhof, Phys. Rev. Lett. 77 (1996) 3865.
[23] A.M. Mills, A. Mar, J. Am. Chem. Soc. 123 (2001) 1151.
[24] G. Cordier, H. Schäfer, M. Stelter, Z. Naturforsch. 40b (1985) 5.
[25] H.L. Clark, H.D. Simpson, H. Steinfin, Inorg. Chem. 9 (1970) 1962.
[26] K. Deller, B. Eisenmann, Z. Naturforsch. 31b (1976) 29.
[27] A. Rohr, S.M. Kauzlarich, Acta Crystallogr. C 50 (1994) 1859.
[28] A.M. Mills, A. Mar, Inorg. Chem. 39 (2000) 4599.
[29] J.S. Smart, Effective Field Theories of Magnetism, Saunders, Philadelphia, PA, 1966.
[30] H. Li, C.Y. Wu, J.C. Ho, Phys. Rev. B 49 (1994) 1447.
[31] A. Ochiai, E. Hotta, Y. Haga, T. Suzuki, O. Nakamura, J. Magn. Magn. Mater. 140 (1995) 1249.